Original Paper

Visualization of adaptive polymer flow and displacement in medium-permeable 3D core-on-a-chip

Yan Zhang [a], Xue-Zhi Zhao [a], Pei-Hui Han [b], Li-Yuan Zhang [c, d], David A. Weitz [c], Yu-Jun Feng [a, *]

[a] Polymer Research Institute, State Key Laboratory of Polymer Materials Engineering, Sichuan University, Chengdu, 10065, Sichuan, PR China
[b] EOR Laboratory, Exploration & Development Research Institute, Daqing Oilfield Limited Company, PetroChina, Daqing, 163712, Heilongjiang, PR China
[c] School of Engineering and Applied Sciences, Harvard University, Cambridge, 02138, United States
[d] School of Petroleum Engineering, China University of Petroleum, Qingdao, 266580, Shandong, PR China

A R T I C L E   I N F O

A B S T R A C T

Polymer flooding has been witnessed an effective technology for enhancing oil recovery from medium-to low-permeability reservoirs; however, direct visualization of polymer solution flow in such reservoir condition is still lacking. In this work, a three-dimensional (3D) core-on-a-chip device with a permeability of around 200 mD was prepared and employed to visualize the pore-scale flow and displacement of a self-adaptive polymer (SAP, 8.7×10^6 g•mol^{-1})–whose microscopic association structure and macroscopic viscosity can reversibly change in response to shear action–versus partially hydrolyzed polyacrylamide (HPAM), by recording their flow curves, monitoring dynamic transportation process via particle imaging velocimetry, and building 3D structure of remaining oil. The results show that, in single-phase flow, all polymer solutions exhibit flow thinning and then thickening regions as flow rate increases, but the transition between two regimes occurs at a small Weissenberg number (10^{-3}–10^{-1}) in this medium-permeable condition. In contrast to HPAM-1 with close weight-average molecular weight (M_w), the adaptive character not only extends SAP's shear-govern region, allowing SAP to propagate piece by piece and achieve higher accessible pore volume, but it also enhances the elastic resistibility of polymer in the extension-dominated regime, increasing the microscopic displacement efficiency. These two effects result in 1.5–3 times more oil recovery factor for SAP than for HPAM-1. Regarding ultra-high-M_w HPAM-2 (25×10^6 g•mol^{-1}), plugging and chain degradation do occur, thus producing lower oil recovery than SAP. This work provides a direct approach for in-situ assessment of polymer-based displacing system under a more authentic condition of practical reservoirs.

1. Introduction

To date, oil still accounts for the largest share of global primary energy demand, reaching 31% in 2021 (BP p.l.c., 2022). The remaining proved oil reserves are 1.732 trillion barrels by the end of 2020, with levels as high as 67% being medium- and low-permeability resources. Many pilot tests (Jones, 1963; Pu et al., 2008; Haynes et al., 2013; Bennetzen et al., 2014; Leon et al., 2018) around the world have witnessed that polymer flooding is potentially effective for incremental oil production in medium-to low-permeability oil reservoir. However, there is still lack of the direct monitoring of the flow of polymer solutions in such reservoir conditions.

As a leading chemically enhanced oil recovery (EOR) technology, polymer flooding has already achieved great success throughout the world, especially in China, since its initial practice in the early 1960s. Daqing Oilfield, remaining the world's largest polymer application, started a feasibility study of polymer flooding in 1965 and implemented scale-up field application thirty years later (Zhang et al., 2021). Hitherto more than 10 million tons of annual oil production has been sustaining for 18 consecutive years, with around cumulative 14% of original oil in place (OOIP) from polymer EOR. Nevertheless, with the extension of polymer flooding from these relatively high-permeability oil formations to those with the

Please cite this article as: Y. Zhang, X.-Z. Zhao, P.-H. Han et al., Visualization of adaptive polymer flow and displacement in medium-permeable 3D core-on-a-chip, Petroleum Science, https://doi.org/10.1016/j.petsci.2022.10.013

average permeability (K) less than 200 milliDarcy (mD), lower recovery factor, 4%−10.2% OOIP, was obtained. This is because the commonly used high-molecular-weight (high-M_{w}) partially hydrolyzed polyacrylamide (HPAM) faces challenges in such low-permeability oil layers.

Polymer performance in porous media flow is well known to be highly susceptible to shear and extension forces, which are amplified for decreasing pore throats as medium permeability declines (Smith, 1970; Sorbie, 1991; Seright, 1983). Therefore, high-M_{w} HPAM due to large molecular size cannot be smoothly injected into the medium-to low-permeable formations; if it is forced to be injected, the flexible long chains would be devastated mechanically, resulting in irrevocable loss in polymer solution viscosity. To overcome the unsatisfactory injectivity of HPAM and to guarantee high viscosity for polymer solution, we earlier proposed a relatively low-M_{w} (~8 × 10^{6} g•mol^{-1}) self-adaptive polymer (SAP) for medium-to low-permeability exploitation (Zhang et al., 2019). For such type of polymer, apart from the same entanglements as HPAM, physical aggregates are formed by the hydrophobic side chains from different water-soluble skeletons above a critical polymer concentration (C_{p} = 854 mg•L^{-1}); this non-covalent connection is easily disassembled and reorganized when external stresses change reversibly, behaving the adaptive feature. Both our work and preceding researches (Chissonde et al., 2021; Dupuis et al., 2011; Guo et al., 2016, 2017; Wang et al., 2021) have verified in laboratory investigation that this class of hydrophobically modified acrylamide-based polymers can gain higher oil recovery compared against conventional polymers. Furthermore, our SAP polymer has been extended from laboratory synthesis to scale factory pilot manufacturing, and the pilot test of such pilot product was carried out in 25 wells (9 injection and 16 production wells) of Daqing oilfield in 2018, with a yearly dosage of 105 tons of powder and a daily oil increase of 1.0 ton per well. Despite this class of smart polymers has opened a new pathway for EOR in medium-to low-permeability reservoirs, how they propagate and why they displace oil in porous media with such permeability range are unclear yet, because typical porous media such as sand pack columns, artificial cores, and natural rocks are opaque to visible light, precluding the direct visualization of fluid flow dynamics inside them.

During the last two decades, microfluidics-based transparent models have been developed to study the pore-scale flow of complex fluid under transient conditions (Browne et al., 2020), represented by the regular expansion-contracting geometry (Rodd. et al., 2007; Galindo-Rosales et al., 2012; Ober et al., 2013) and the disorder etching channel based on realistic core (Nilsson et al., 2013; Zhao et al., 2022) at two-dimensional (2D) scale. However, those 2D micromodels cannot reflect the complex connectivity and tortuosity of real-world porous media in the third dimension, which is always a critical factor affecting the flow of polymer solution. A 3D micromodel can thus better mimic the 3D geometric features of natural porous media (Karadimitriou and Hassanizadeh, 2012; Anbari et al., 2018). In such core-on-a-chip model, uniformly or multiple-sized glass beads were randomly packed and sintered in a quartz capillary without deterioration of their original shape. By closely matching the refractive index between medium matrix and fluids, one can observe the fluid flow inside 3D media under a confocal microscope and reorganize the 3D structure of mobile phase. This technique has been successfully harnessed to examine the breakup and mobilization of nonwetting fluid (Datta et al., 2014a, b), displacement of trapped fluid (Krummel et al., 2013; Zhao et al., 2022; Browne et al., 2020), and polymer solution flow in porous media (Datta et al., 2013; Parsa et al. 2020, 2021; Browne and Datta, 2021). Nevertheless, the permeability of the model cores in those literatures, measured using Darcy's law or theoretically predicted from the Kozeny-Carman relation, were in the range

of 1−100 D, much higher than those of the medium-to low-permeable reservoirs, i.e., K < 500 mD (China National Energy Administration, 2021).
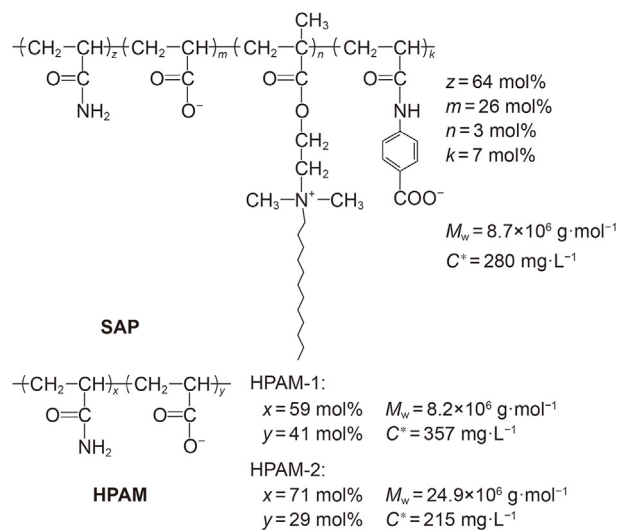
Keeping all of the foregoing in mind, in this work, we fabricated a medium-permeable 3D transparent porous media; within it the flow and displacing behaviors of SAP were visually examined, and compared with its M_{w}-equivalent counterpart, HPAM-1, and an ultra-high-M_{w} reference, HPAM-2, thus shedding light on the origin of its effective enhanced oil recovery in such permeability condition. The macroscopic flow resistance of polymer solution in porous media was represented by the effective viscosity, which was related to the bulk rheological performances that are characterized with shear and elongational rheometers. With respect to the microscopic displacement, we employed particle image velocimetry (PIV) strategy to detect the pore-scale velocity of polymer solution in real time, thus to monitor its dynamic transportation process. Finally, polymer enhanced oil recovery tests were implemented in the micromodel, in which the pore-level residual oil distribution was constructed to analyze the difference in oil displacement among three polymers. All the experiments were proceeded under the reservoir condition of Daqing oilfield, which has a temperature of 45 °C and a saline solution of 4500 mg•L^{-1} NaCl.

2. Materials and methods

2.1. Materials

The SAP polymer, consisting of acrylamide, sodium acrylate, hydrophobic monomer, and rigid unit, was prepared in our laboratory. HPAM-1 and HPAM-2 were kindly offered by Daqing Oilfield Company, China. Their architectures and structural parameters were well characterized in our previous work (Zhang et al., 2019) and are displayed in Scheme 1.

We investigated five groups of polymer solutions: (i) SAP, C_{P} = 1000 mg•L^{-1}; (ii) HPAM-1, C_{P} = 1000 mg•L^{-1}; (iii) HPAM-2, C_{P} = 1000 mg•L^{-1}; (iv) HPAM-1, C_{P} = 1250 mg•L^{-1}; (v) HPAM-2, C_{P} = 750 mg•L^{-1}. All the test solutions span a range of 2.8−4.7 for the ratio of polymer concentration to overlap concentration (C_{P}/ C^{*}), i.e., in the semi-dilute regime. In particular, the three polymer solutions in groups (i), (iv), and (v) have close shear viscosity

SAP

z = 64 mol%
m = 26 mol%
n = 3 mol%
k = 7 mol%

M_{w} = 8.7×10^{6} g·mol^{-1}
C^{*} = 280 mg·L^{-1}

HPAM

HPAM-1:
x = 59 mol% M_{w} = 8.2×10^{6} g·mol^{-1}
y = 41 mol% C^{*} = 357 mg·L^{-1}

HPAM-2:
x = 71 mol% M_{w} = 24.9×10^{6} g·mol^{-1}
y = 29 mol% C^{*} = 215 mg·L^{-1}

Scheme 1. Chemical structure and structural parameters of polymers in 4500 mg•L^{-1} NaCl solution at 45 °C.
M_{w} and C^{*} represent weight-average molecular weight and overlap concentration of polymer, respectively.

Y. Zhang, X.-Z. Zhao, P.-H. Han et al.

(~18 mPa•s) at a representative shear rate (10 s^{-1}) of real field pilot, as well as similar $C_P/C^* \approx 3.5$.

Analytical-grade NaCl (Chron Chemicals, Chengdu, China), carboxylate-modified polystyrene latex beads (2.5% aqueous suspension, Sigma, USA), fluorescein (99%, J&K, China), formamide (AR, Chron Chemicals, Chengdu, China), dimethyl sulfoxide (DMSO, 99.7%; Adamas-beta, China), nile red (99%, Sigma, USA), rhodamine B (BS; Adamas-beta, China) were used as received. Deionized water with resistivity of 18.25 MΩ•cm was produced from an ultrapure water purification system (UPH–I-10T, Ulupure, Chengdu, China). Paraffin oil (No. 15) was purchased from Lingzhong Lubricating Oil Co., Ltd. (Chengdu, China) and filtered through 0.8-μm Millipore filter prior to use. Crude oil, having a shear-independent viscosity of 11 mPa•s at 45 °C, was originated from Daqing Oilfield Company and eliminated impurity through vacuum suction filtration.

2.2. Preparation of polymer solutions

Designated amount of NaCl powder was dissolved in deionized water to obtain NaCl aqueous solution. Two kinds of polymer solutions were prepared: (i) direct dissolution of designed amount of polymer powder into 4500 mg•L^{-1} NaCl aqueous solution forms polymer aqueous solution; (ii) polymer mother solution was primarily readied with the method (i), and then diluted with formamide and DMSO to gain a polymer solution whose refractive index is precisely matched to that of the glass beads; the final polymer solution consists of 63 wt% formamide, 27 wt% DMSO, 9.55 wt% water, and 0.45 wt% NaCl, and has a measured refractive index of 1.47. We also prepared an index-matching saline water without polymer following the same procedure as (ii).

2.3. Bulk rheology

Shear rheology of polymer solution was characterized on a Physica MCR 302 (Anton Paar, Austria) rotational rheometer at 45 °C. A Searle-type concentric cylinder geometry CC27 was used during a shear sweep from 0.01 to 1000 s^{-1}. The radii of the measuring bob and measuring cup are 13.33 and 14.46 mm, respectively. A cone-and-plate geometry (CP50-1) with diameter of 50 mm and cone angle of 1° was employed in a vicinity of shear rates, 0.01−2000 s^{-1}, and the gap between cone and plate was set to 0.1 mm for all the measurements.

The extensional response of polymer solution was detected at 45 °C on a dripping-onto-substrate (DoS) rheometry set-up (Dinic et al. 2015, 2017). Polymer solution was injected into a tube using a syringe pump (LSP01, Langer pump, China) at 0.02 mL•min^{-1}. When the liquid released from nozzle hits the glass slide, the pump was shut off, and simultaneously the formation and evolution of the liquid necking were captured at a rate of 20,000 frames per second using a high-speed camera (Fastcam Mini UX50, Photron, Japan). The distance between the nozzle and glass slide was kept constant at 1.83 times the nozzle's diameter (1.28 mm).

2.4. Fabrication and physical characteristics of porous medium

A rigid 3D porous medium used for core-like flooding was made as follows. Glass microspheres with diameter $D_{gm} = 19$ μm (SIMT, Shanghai, China) were randomly packed into a thin-walled rectangular quartz capillary (DIFU, China) having a square cross section of area $A = 3$ mm by 3 mm. We then tapped the packed tube for 3 min to densify, and then lightly sintered the medium in a furnace at 980 °C for 5 min. Finally, the ends of the packing were equipped with tubing and sealed with epoxy glue (Fig. 1a). The length of the device along the flow direction is $L \approx 8$ cm. We determined the medium porosity $\phi = 27 \pm 2\%$ by addressing the confocal image
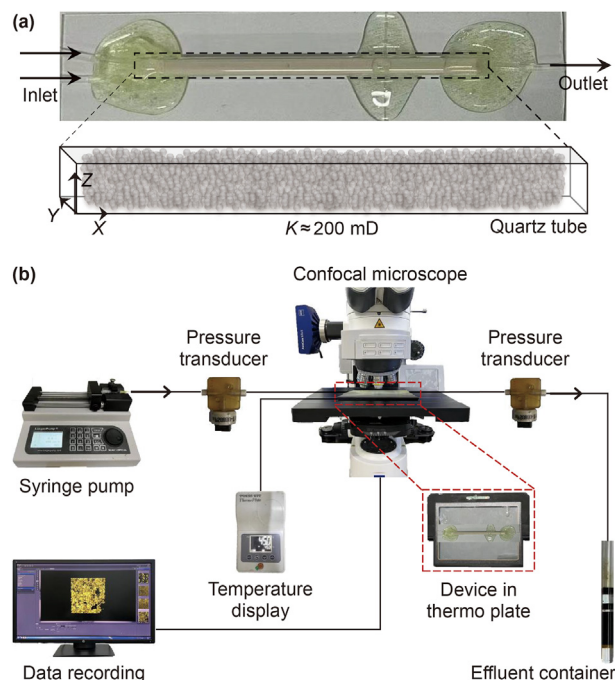

Fig. 1. Schematic of 3D transparent micromodel (**a**) and the experimental apparatus (**b**).

using ImageJ software (Fig. S1 in Electronic Supplementary Material), and measured permeability $K = 200 \pm 50$ mD based on Darcy's law. Prior to injecting any fluid, we removed air from the whole device under vacuum for 24 h and then filled with CO_2.

2.5. In-situ rheology in porous medium

We characterized the rheology *in-situ* by injecting the target fluid into the 3D medium at 45 °C, over a range of volumetric flow rate Q, and acquiring the corresponding steady-state pressure drop (ΔP) across the medium with a pressure transducer (UPS01-T1, Labsmith, USA) (see Fig. 1b). The corresponding interstitial shear rate of porous medium ($\dot{\gamma}_{pm}$) at each flow rate can be calculated from the following expression (Sorbie, 1991; Chauveteau, 1982):

$$\dot{\gamma}_{pm} = \frac{4\alpha u}{\sqrt{8K/\phi}} \tag{1}$$

where $\alpha = 1.25$ for the spherical glass bead pack with $D_{gm} = 10-20$ μm (Chauveteau, 1982), and $u = Q/(\phi A)$ is the average velocity. The Q and corresponding $\dot{\gamma}_{pm}$ values for all flow groups are shown in Fig. S2 in Electronic Supplementary Material.

Concerning the flow in porous media, the Reynolds number comparing inertial to viscous stresses was defined as $Re = \rho(Q/\phi A)d_t/\eta$ (Browne and Datta, 2021), where ρ and $d_t = 0.16D_{gm}$ are the density of fluid and pore throat diameter, respectively. For accuracy, we used the rate-dependent shear viscosity $\eta_s(\dot{\gamma})$ in this calculation, as a result, Re in our experiments ranges from 1.7×10^{-9} to 8.1×10^{-4}; such small values indicate that both solvent and polymer solution flows are laminar. Therefore, Darcy's law, $\eta/\Delta P = KA/(QL)$, was employed to describe these flows, which offers a direct mapping from the ΔP to the η because all the other parameters are independently known. In this case, injecting solvent and polymer solution into the same medium at the identical Q generates $\eta_w/\Delta P_w = \eta_p/\Delta P_P$, therein $\eta_w \approx 0.6$ mPa•s at 45 °C and is rate-independent. The effective

viscosity of polymer solution *in-situ* was thus obtained from $\eta_{\text{eff}} = \eta_{\text{w}}(\Delta P_{\text{P}}/\Delta P_{\text{w}})$.

2.6. Particle imaging velocimetry (PIV)

Carboxylate-modified polystyrene latex beads ($D_{\text{fb}} = 200$ nm in diameter) serving as flow tracers were dispersed in refractive index-matching brine and index-matching polymer solution at 0.002% by volume. Flow tests comprise sequentially injecting index-matching brine, index-matching polymer solution, and index-matching brine again at 45 °C. The volumetric flow rates of all stages were set to keep $\dot{\gamma}_{\text{pm}} = 10$ s^{-1}, and their specific values are listed in Table S1 in Electronic Supplementary Material. At these flow rates, diffusion of the tracer particles is negligible because their Peclet number, the relative strength of advection to diffusion, is of the order of 10^2. In each flow sequence, we chose a *XY* position at the focal plane and tracked particles movement at 3 frames per second for 5 min using a confocal microscope (Zeiss LSM 700, Germany). Images were then treated using ImageJ and MATLAB software as reported previously (Datta et al., 2013; Parsa et al., 2021) to obtain the pore-level velocities.

2.7. Multiple-phase displacement in porous medium

The multiple-phase displacement tests in micromodel were conducted at 45 °C as described in core flooding operations (Li et al., 2017). Five models were prepared, and their basic parameters are listed in Table S1 of Supporting Information. The model was first saturated with oil, and then sequentially displaced using water, polymer solution, and water. The pressure drops over time during each run were recorded with the pressure transducer as mentioned in Section 2.5. The confocal images were captured at a series of *Z* positions under 488 nm excitation, and further analysed by ZEN program.

The oil recovery is the volume of the accumulated oil production divided by the initial saturation, and is usually expressed as a percentage; the total oil recovery in the entire flooding process minus the initial water flooding recovery (E_{w}) before polymer injection is the incremental oil recovery by the polymer solution (E_{p}) (Zhao et al., 2013).

3. Results and discussion

3.1. Bulk rheological properties of polymer solutions

The viscosity of the polymer, particularly its fluctuations with deformation rate, is the major solution property of interest during polymer flooding. Because the flowing medium has complicated geometries, most practical polymer solution flows include shear and elongational components (Sochi, 2010). In this section, we therefore separately executed the sole shear and extension flow of polymer solution in a well-defined geometry of viscometers, and examined their bulk rheological responses to anticipate the flow behavior in porous medium.

3.1.1. Shear rheology

First, steady shear flow curves were inscribed using the concentric-cylinder geometry, with stepwise increasing shear rates ($\dot{\gamma}$) from 10^{-2}–10^3 s^{-1} (Fig. S3a in Electronic Supplementary Material). Similar to observation in our preceding work (Zhang et al., 2019) and also to most pioneer reports (Sorbie, 1991; Wever et al., 2011), all polymer solutions successively show a Newtonian region (i.e., a constant viscosity) and a shear thinning regime upon increasing shear rate. In the domain of $\dot{\gamma} > 200$ s^{-1}, instead of a

second Newtonian plateau, all curves exhibit shear thickening behavior. This abnormal stage is often considered as an artifact due to the inertial Taylor instability in the cylinder configuration (Mezger, 2020), here, thus hindering the viscosity characterization of polymer solutions at high shear rates.

To overcome this problem, we employed a classical cone-and-plate geometry, with which high shear rate can achieve for low-viscosity fluid at small gap height (<100 μm) (Pipe et al., 2008), to perform the step shear rate tests ranging from 10 to 2000 s^{-1} (Fig. S3b in Electronic Supplementary Material). In this shear rate range, SAP and HPAM-2 solutions have a noticeable second Newtonian viscosity, whilst the relatively low-M_{w} HPAM-1 solutions merely exhibit a decreasing viscosity; all plots have no upward tails at high shear rates.

Fig. 2 compares two groups of results, and reveals that viscosity curves in two scenarios can totally overlap at $\dot{\gamma} < 200$ s^{-1} for all polymer solutions, indicating the consistency of two approaches. By integrating data from both cases, the plots of shear viscosity (η_{s}) versus $\dot{\gamma}$ can be described using the conventional Carreau viscosity equation (Eq. (2)) (Carreau, 1972), thereby introducing several parameters to contrast polymer features quantitatively.

$$\eta_{\text{s}} = \eta_{\infty} + \frac{\eta_0 - \eta_{\infty}}{\left[1 + (\dot{\gamma}/\dot{\gamma}_{\text{c}})^2\right]^{(1-n)/2}} \tag{2}$$

where η_0 and η_{∞} represent the zero-shear and infinite-shear viscosities, respectively, mPa·s; $\dot{\gamma}_{\text{c}}$ denotes the characteristic shear rate for the onset of shear thinning; and *n* refers to the power-law exponent.

All the parameters presented in Table 1 verify the following distinction among three polymer solutions: (i) under the same concentration condition (row 1–3), η_0 and η_{∞} for SAP is higher than that for HPAM-1, and both of them are much lower than that for high-M_{w} HPAM-2; this verdict is also true for their η_{s} trend in the whole range of shear rates. In our previous work (Zhang et al., 2019), we proved that the difference between SAP and M_{w}-equivalent HPAM-1 stems from the former polymer's structural viscosity due to the association aggregates; the fact $\dot{\gamma}_{\text{c}}$ (SAP) $< \dot{\gamma}_{\text{c}}$ (HPAM-1) further verifies that the adaptive aggregate of SAP is more sensitive to shear action than chain entanglements. (ii) Among polymers with the comparable shear viscosity at 10 s^{-1} (row 1, 4 and 5), HPAM-2 solution with reduced concentration of 750 mg•L^{-1} still owns the largest η_0 value, consecutively followed by SAP and HPAM-1 ($C_{\text{HPAM-1}} = 1250$ mg•L^{-1}), whereas its viscosities at shear rate beyond 10 s^{-1} is lower than the latter two solutions (Fig. 1b); this should be attributed to the magnificent shear sensitivity for high-M_{w} HPAM (Wu, 2013; Martínez Narváez et al., 2021). (iii) $n < 1$ for all the polymer solutions claims their characterics of power law fluid; SAP has a smaller *n* than HPAM-1 but a larger value than HPAM-2, re-confirming that it is superior to HPAM-1 but inferior to HPAM-2 in terms of shear susceptibility. Moreover, we notice that polymer concentration imparts no effect on this nature.

3.1.2. Extensional rheology

The pure extensional rheology response of polymer solutions was determined using the recently developed dripping-onto-substrate (DoS) rheometry, which relies on the pinching dynamics of fluid necking thread to judge polymer viscoelasticity and can apply to weak elastic polymer solution with η_{S} less than 20 mPa•s (Dinic et al., 2015).

The neck pinch-off processes of SAP, HPAM-1, and HPAM-2 solutions are played in the Movie S1 and S2 (see the Supporting Information), which can be divided into two distinct regimes as reported antecedently (Smith, 1970; Dinic et al. 2015, 2017): (i)
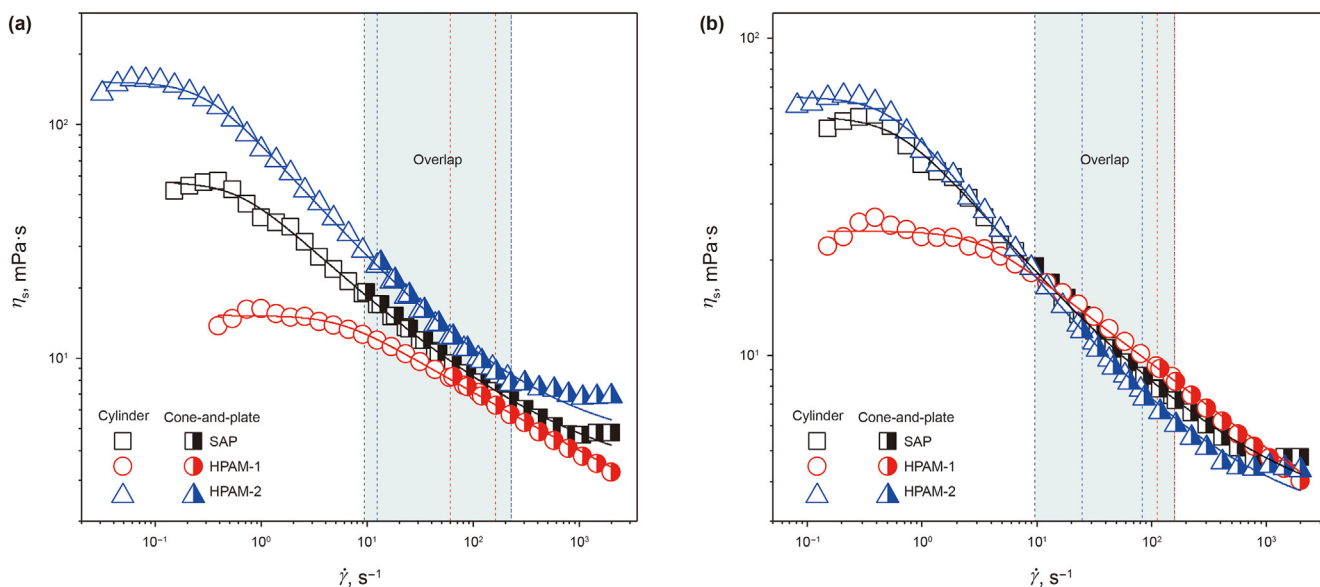
Fig. 2. Bulk rheological response of polymer solutions to pure shear flow at 45 °C is represented by variation of shear viscosity (η_s) as a function of shear rate ($\dot{\gamma}$). (**a**) $C_p = 1000$ mg•L^{-1} for three polymer solutions. (**b**) $C_{SAP} = 1000$ mg•L^{-1}, $C_{HPAM-1} = 1250$ mg•L^{-1}, and $C_{HPAM-2} = 750$ mg•L^{-1}. The dotted rectangles show the overlap of cylinder-geometry results and cone-and-plate-geometry findings. Solid lines are the fittings based on Carreau model. Solvent, 4500 mg•L^{-1} NaCl aqueous solution.

Table 1
Shear and extensional rheological parameters for SAP, HPAM-1, and HPAM-2 at 45 °C in 4500 mg•L^{-1} NaCl aqueous solution.

Sample	C_p, mg•L^{-1}	η_0, mPa·s	η_∞, mPa·s	$\dot{\gamma}_c$, s^{-1}	n	G_e, mPa	τ_e, ms
SAP	1000	56.7	2.8	0.62	0.55	2177	6.96
HPAM-1	1000	15.2	0.6	5.59	0.72	930	0.54
HPAM-2	1000	152.1	4.0	0.30	0.47	3369	9.98
HPAM-1	1250	24.7	0.6	3.20	0.71	3061	4.15
HPAM-2	750	65.4	2.7	0.58	0.49	1099	5.88

inertial and capillary stresses impel the droplet to descend and evolve into a neck shape between the nozzle and glass slide; (ii) the neck thread gradually slenderizes due to the elastic effect of polymer solution, until it is squeezed off. Contrasting the duration of this procedure for three polymers at 1000 mg•L^{-1}, we observed significantly longer filament lifespan for solution of HPAM-2 as against SAP and HPAM-1. However, declining the concentration of HPAM-2 to 750 mg•L^{-1} remarkably accelerate the occurrence of pinch-off event; as a result, its necking filament lasts for less time than SAP yet still for longer duration than HPAM-1 of 1250 mg•L^{-1}, despite their alike shear viscosity. For better quantitative comparison, we define the time for the onset of elastic-dominated regime (t_c) as the starting moment, i.e., $t - t_c = 0$ (Fig. 3a), where a similar initial filament radius is discovered for all systems. In this scenario, at an identical time for example $t - t_c = 30$ ms, it is clear that 1000 mg•L^{-1} SAP solution possesses vigorous elastic resistance to capillary breakage, which is only slightly less than concentration-equivalent HPAM-2 but considerably stronger than that of two HPAM-1 solutions and 750 mg•L^{-1} HPAM-2. More surprisingly, one can obviously find beads-on-a-string morphology for only SAP solution in the last stages of thinning (Movie S1.mp4 and Movie S2.mp4 in Electronic Supplementary Material, and Fig. 3a), which is a well-known feature for low viscosity but highly elastic polymer solutions (Rodd et al., 2005; Oliveira et al., 2006).

Supplementary data related to this article can be found at https://doi.org/10.1016/j.petsci.2022.10.013.

Above image sequences were then converted to the ratio of necking filament radius to initial value ($R_f/R_{f,0}$), as plotted over time

using a logarithmic ordinate in Fig. 3b. Clearly, a sharp transition point (t_c) separates an incipient power law regime from a slower exponential decay, which are corresponding to the aforementioned inertio-capillary and elastocapillary regimes. The latter section for many polymer solutions can be characterized by the single exponential relaxation function (Eq. (3)) (Entov and Hinch, 1997; McKinley, 2005).

$$\frac{R_f(t)}{R_{f,0}} = \left(\frac{G_e R_{f,0}}{2\sigma}\right)^{1/3} e^{\left(-\frac{t}{3\tau_e}\right)} \tag{3}$$

where G_e and τ_e are the apparent elastic modulus and the longest extensional relaxation time, respectively.

As illustrate in Table 1, at $C_p = 1000$ mg•L^{-1}, both G_e and τ_e for SAP are lower than that for HPAM-2, yet much greater than that for HPAM-1, directly indicating the magnitude of their elasticity: HPAM-1 < SAP < HPAM-2. Among the three polymer systems having same shear viscosity, HPAM-1 solution of 1250 mg•L^{-1} has the largest G_e value (3061 mPa), though, its τ_e remains minimal (4.15 ms). These results suggest, for flexible HPAM polymer, the higher the M_w and the C_p, the stronger is the elasticity of the polymer and the longer it takes for the polymer chain to restore to its equilibrium state after being disrupted. By contrast with polymer concentration, molecular weight is more crucial in determining the relaxation time, in good agreement with literature consequence (Martínez Narváez et al., 2021). For M_w-equivalent analogues, SAP's dominant elastic character over HPAM-1 derives from the strong resistive strength of intermolecular attractions between hydrophobic chains to extensional action, which is consistent with our pervious analysis (Zhang et al., 2019) based on CaBER extensional rheometer data, as well as to what reported by Azad et al. (2018) recently.

Following the standard practice for extensional rheology characterization (Dinic et al., 2017; Rodd et al., 2005; McKinley, 2005), the evolution of necking filament radius with time in the elastocapillary regime can be further transformed to the apparent extensional viscosity (η_e) as a function of Hencky strain, $\varepsilon = 2\ln(R_{f,0}/R_f(t))$, using Eq. (4).
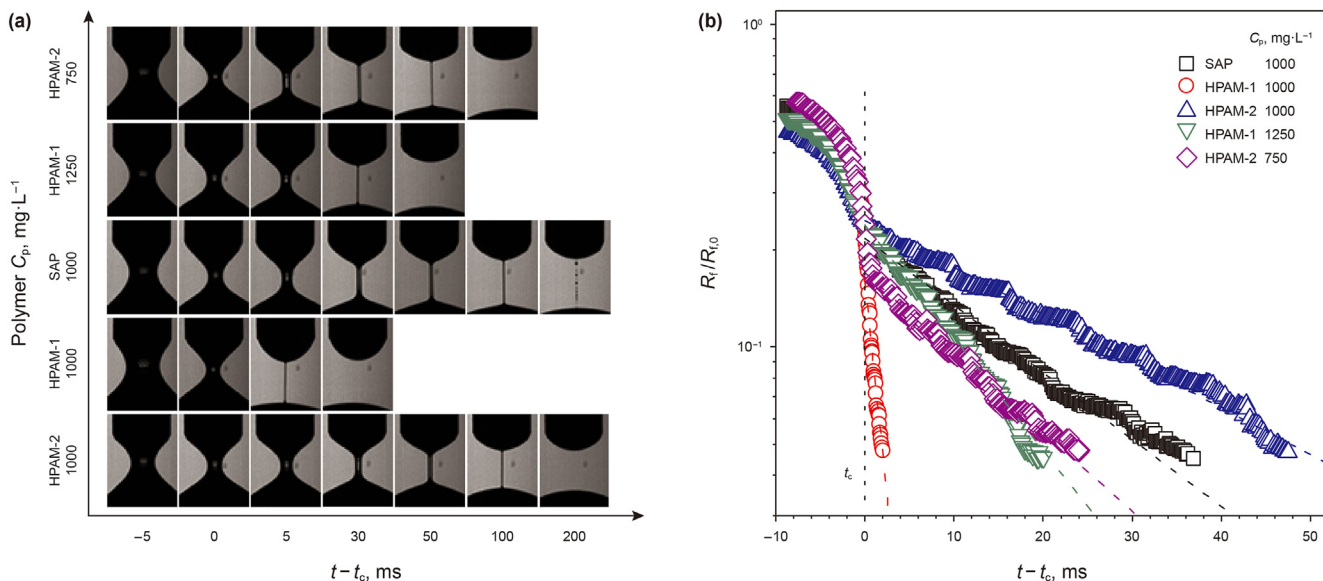
Fig. 3. Necking filament shape and radius evolutions of SAP versus HPAM polymers in 4500 mg•L^{-1} NaCl aqueous solution at 45 °C. (**a**) Representative images of neck-filament thinning and pinch-off dynamics. (**b**) Ratio of necking filament radius (R_f) to initial value ($R_{f,0}$) plotted as a function of time (t). t_c is a transition time, beyond which the elastic effect of polymer solution governs thinning dynamics.

$$\eta_e = \frac{\sigma}{R_f(t)\dot{\varepsilon}} \quad (4)$$

where σ is the surface tension of polymer solution at 45 °C; $\dot{\varepsilon}$ denotes the extension rate of the fluid filament, given by $\dot{\varepsilon} = -\frac{2}{R_f(t)}\frac{dR_f(t)}{dt}$.

As displayed in Fig. 4, all polymer solutions exhibit strain-hardening behavior, as opposed to the pure thinning behavior in the shear field; as a result, high ratios ($Tr = \eta_e/\eta_s$), 10^2–10^3, are received when $\eta_s = \eta_{10}$. Comparatively, the η_e values for five polymer systems are in the descending order of HPAM-2 (1000 mg•L^{-1}) > SAP (1000 mg•L^{-1}) ≈ HPAM-2

Fig. 4. Transient extensional viscosity (η_e) plotted as a function of Hencky strain (ε) for polymers in 4500 mg•L^{-1} NaCl aqueous solution. T = 45 °C.

(750 mg•L^{-1}) > HPAM-1 (1250 mg•L^{-1}) > HPAM-1 (1000 mg•L^{-1}), giving a prediction for the magnitude degree of flow resistance of these polymer solutions in porous media.

3.2. In-situ rheology of polymer solutions flowing through 3D porous media

From Section 3.1, we conclude that high-M_w HPAM-2 shows susceptive response to sole shear, but powerful resistance to pure extension, as opposed to the case of relatively low-M_w HPAM-1. The adaptive peculiarity of SAP as stated in the Introduction part enhances its shear sensitivity as well as extension resistibility, which is greater than those of M_w-equivalent HPAM-1, either at the same concentration or close viscosity. We now consider whether these regularities are equal in disordered 3D porous media, where polymer solution always undergoes a complicated flow of shear and elongation (González et al., 2005).

We primarily quantified the macroscopic flow resistance of polymer solutions for single-phase flowing through porous media, which is represented by the effective viscosity (η_{eff}) and displayed in Fig. 5a as a function of the average shear rate ($\dot{\gamma}_{pm}$) of medium. For all polymer solutions, the η_{eff} exhibits a similar flow-thinning regime as the bulk shear rheology at the relatively low flow rates, succeeded by an increase above a critical $\dot{\gamma}_{pm,c}$. In the former flow-thinning zone, the flow curves of SAP and HPAM-1 almost overlap with their bulk rheological profiles, whereas the η_{eff} of HPAM-2 solution is always higher than its bulk shear viscosity at the same shear rate; the vertical shifts between viscosity curves for HPAM-2 may be due to adsorption or slight clogging (Skauge et al., 2018). In the latter flow thickening regime that generally defined as the extensional dominant flow (Sochi, 2010; Wu, 2013; Stavland et al., 2010; Seright et al., 2011; Skauge et al., 2018; Azad and Trivedi, 2019), η_{eff} of SAP and HPAM-1 eventually saturates at a maximum value for $\dot{\gamma}_{pm} \approx 5 \dot{\gamma}_{pm,c}$. In stark contrast to those low-M_w polymers, the η_{eff} of high-M_w HPAM-2 solutions hits a peak, subsequently followed by a decreasing viscosity interval before reaching a steady value. This phenomenon can be interpreted as high viscoelastic stresses causing polymer rupture and chain halving
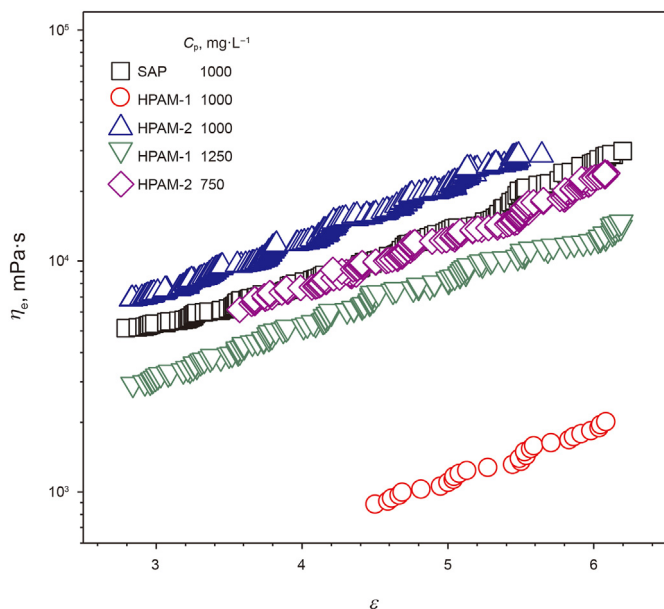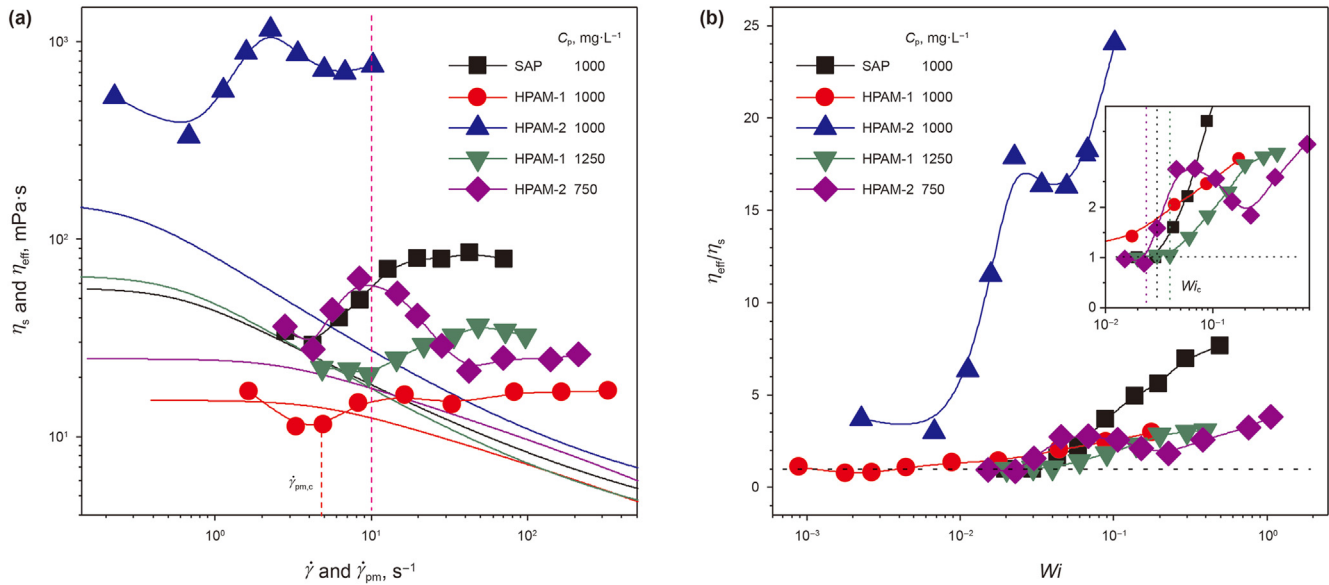
Fig. 5. Characterization of macroscopic flow resistance for SAP, HPAM-1, and HPAM-2 solutions in 3D transparent porous media at 45 °C. (**a**) The *in-situ* viscosities (η_{eff}) plotted as a function of the average shear rate of porous medium ($\dot{\gamma}_{pm}$), which are compared with the bulk rheological curves (η_s–$\dot{\gamma}$, solid lines). (**b**) The reduced apparent viscosity (η_{eff}/η_s) plotted as a function of the Weissenberg number (Wi). The solvent of polymer solutions is 4500 mg•L^{-1} NaCl aqeous solution.

(Skauge et al., 2018), and it has been observed to being more severe in polymers of ultrahigh M_w as well as low-permeability porous environments (Hatzignatiou et al., 2013).

Since the extension-governing flow is driven by the elasticity of polymer solutions (Ranjbar et al., 1992), we further use the Weissenberg number (Wi), comparing elastic to viscous stresses, to characterize the pore-scale transition to elongational flow. This dimensionless parameter defined as a ratio between the characteristic relaxation time of a fluid and characteristic time of porous media is expressed as $Wi = \dot{\gamma}_{pm} \cdot \tau_e$ (Ibezim et al., 2021), and correlated to the reduced viscosity (η_{eff}/η_s) of polymer solutions, as shown in Fig. 5b. At low Wi, the flow is laminar with $\eta_{eff}/\eta_s \approx 1$, nearly akin to bulk shear flow; upon a critical Weissenberg number, Wi_c, symbolizing the onset of extension-dominating flow, the ratio of η_{eff} to η_s is higher than 1, and the extensional viscosity takes effect. However, it should be noted that all Wi_c values in the present work, ranging from 10^{-3} to 10^{-1}, are less than 0.5, a general value reported in the literature (Sousa et al., 2018). This deviation is attributed to the relatively low permeability and complicated 3D structure of the medium, as Zamani et al. (2015) proved that the dilatant behavior in a more tortuous rock sample with lower permeability and porosity commences at lower velocity, corresponding to smaller Wi value.

In the same medium sample, i.e., regardless of porous media properties, the variability in Wi_c for five polymer systems indicates an expected consequence that the occurrence of extensional-govern flow is significantly dependent on polymer molecular structure, relative molar mass, and concentration. At $C_p = 1000$ mg•L^{-1}, $Wi_c = 0.03$ for SAP is higher than that for HPAM-1 and HPAM-2 solutions, revealing its wide shear-governing flow zone, which benefits from its adaptive trait, i.e., shear-sensitive dynamic structure. For HPAM-1, increasing concentration to 1250 mg•L^{-1} can effectively delay the onset of extensional flow, consequently, $Wi_c = 0.04$, exceeding that for SAP; this observation agrees with the outcome of Lewandowska (2007) where higher degree of entanglement in polymer solution from elevated concentration broadens the shear thinning region. Nonetheless, this approach cannot enhance the flow resistance of HPAM-1 to

compete with SAP, which is consistent with the bulk rheological results.

Contrary to HPAM-1, the raise in concentration expedites the flow regime transition of HPAM-2; this result shows that for flexible polymers, chain length (corresponding to relative molar mass) rather than the entanglement structure (corresponding to C_p) determines the viscoelastic flow. Also, for this reason, both HPAM-2 solutions at two concentrations have chain degradation due to long chain length, while the other polymers do not. Prior to chain breakage, long relaxation time for HPAM-2 prevents chain from returning to their equilibrium state between pore throats, and thus stress is stored and accumulated, resulting in steep increases in pressure drop and effective viscosity.

3.3. Mobility control of polymer solutions in 3D porous media

Since the main mechanism of polymer flooding is mobility control, i.e., decrease the mobility of the displacing fluid by thickening the aqueous phase, so as to enlarge the swept volume and improve oil recovery efficiency (Sorbie, 1991), to figure out the effect of above flow difference between polymer solutions on their mobility control *in-situ* is key in understanding SAP migration patterns. We use a particle imaging velocimetry (PIV) strategy to explore the polymer-induced pore-level velocity distribution change with cumulative injection fluid, under a fixed volumetric flow rate (Table S1) that reflects a representative shear rate (10 s^{-1}) of real field condition. At this flow situation as shown in Fig. 4a, we underline that η_{eff} (HPAM-2, 1000 mg•L^{-1}) > η_{eff} (HPAM-2, 750 mg•L^{-1}) ≈ η_{eff} (SAP, 1000 mg•L^{-1}) > η_{eff} (HPAM-1, 1250 mg•L^{-1}) > η_{eff} (HPAM-1, 1000 mg•L^{-1}). These η_{eff} values really reflect the mobility control power of polymer solution, as $\eta_{eff} = \eta_w (\Delta P_p / \Delta P_w)$ and $\lambda_w/\lambda_p = (K_w/\eta_w)/(K_p/\eta_p) = \Delta P_p/\Delta P_w$, where λ_w and λ_p are mobility of water phase and polymer solution, respectively.

To quantify velocity fields during the actual flooding steps, we formulated an index-matching solvent to prepare polymer solution, which allows optical microscopy to directly visualize particle tracers within the medium. Although the bulk rheological

Y. Zhang, X.-Z. Zhao, P.-H. Han et al.

properties of these index-matching polymer solutions have some deviation from those of polymer aqueous solutions (see Figs. S4 and S5 in Electronic Supplementary Material), the magnitude of the difference between five polymer systems, as well as the shear viscosity at 10 s^{-1}, remains the same, indicating that the index-matching polymer solution can be used to replace their aqueous solution for comparative study.

Fig. 6a−e display the spatial distribution of velocities during water flooding, polymer transporting, and post water flushing in a heat map; noticeably, the magnitude of the velocity varies spatially over the pore and temporally with the different fluid injection. During the initial water flooding, there are some areas where velocity is zero for all porous media (label (1) in Fig. 6), which adheres a common fact that low-viscosity fluid does not flow through all the pores (Willhite, 1986). When polymer solution transports fully (label (2) in Fig. 6), we notice that, some pores for media displaced by SAP and two HPAM-2 solutions show decreasing velocities, as opposed to that swept by 1000 mg•L^{-1} HPAM-1; for the case using

1250 mg•L^{-1} HPAM-1 to flood, the overall sweeping zone becomes small, yet pores having larger velocities are significantly more abundant. More velocity distributions for different polymer injection amounts are seen in the Fig. S6 in Electronic Supplementary Material. Compared with polymer flow process, a slight decrease of velocity is found in most pores for SAP and low-concentration HPAM-2 groups at the end of post water flooding (label (3) in Fig. 6); however, in the same period, higher-velocities pores remarkably grow for high-concentration HPAM-1 and HPAM-2 displaced medium. Interestingly, post water flooding in the medium that modified by 1000 mg•L^{-1} HPAM-1 solution, makes flow velocities of some pores larger, while others lower.

According to $u_i = Q/(\phi A)$, these velocities variation actually reflect the change of real-time porosity (ϕ_{real}) through which the polymer can flow, because Q and A remain constant. From the perspective of polymer flooding mechanism, mobility control should increase the accessible pore volume and consequently expand ϕ_{real}. Additionally, polymer adsorption onto the rocks could
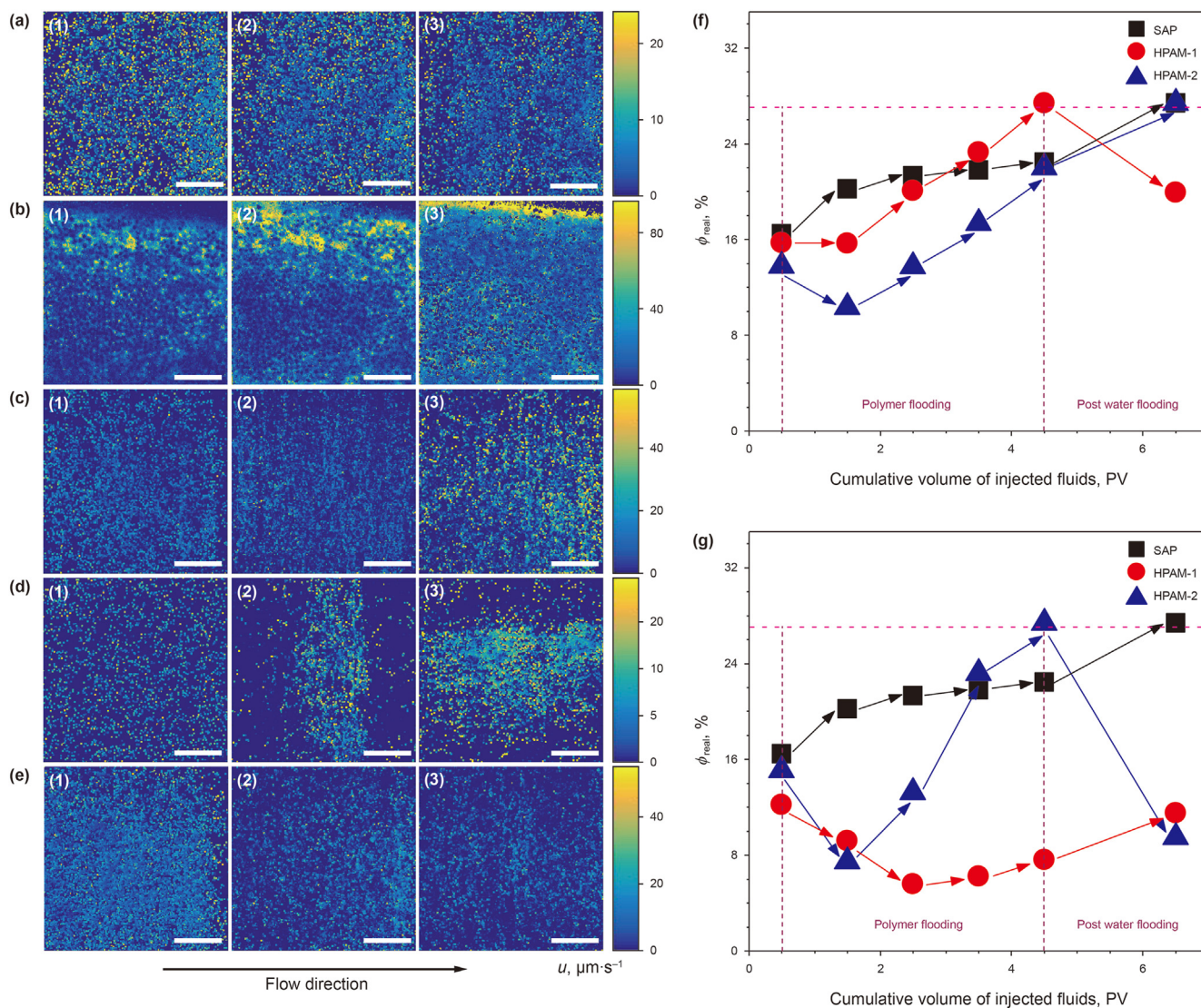

Fig. 6. Mobility control patterns for polymer solutions are characterized by the change in velocity (u) and average real-time porosity (ϕ_{real}) during actual flooding steps at 45 °C. (**a**−**e**) Heat map of magnitude of the fluid velocity in a 2D plane within the 3D porous medium during (1) water flowing, (2) polymer flooding, and (3) post water flushing, for (**a**) SAP ($C_P = 1000$ mg•L^{-1}), (**b**) HPAM-1 ($C_P = 1000$ mg•L^{-1}), (**c**) HPAM-2 ($C_P = 1000$ mg•L^{-1}), (**d**) HPAM-1 ($C_P = 1250$ mg•L^{-1}), and (**e**) HPAM-2 ($C_P = 750$ mg•L^{-1}) solutions. The scale bar is 200 μm. Variation of ϕ_{real} as a function of cumulative volume of injected fluids for (**a**−**c**) groups is shown in (**f**), and for (**a**, **d**, and **e**) groups plotted in (**g**). Water here refers to the index-matching brine consisting of 63 wt% formamide, 27 wt% DMSO, 9.55 wt% water, and 0.45 wt% NaCl, which is also the solvent of polymer solutions.

lower the permeability of rocks to water, which causes a diminution in throat size and therefore ϕ_{real} value (Thomas, 2016). Hence, we compute the ϕ_{real} of all displacement procedures based on the real-time average velocity, and elaborate the differences of mobility control between five displacing fluids by comparing their change profile of ϕ_{real}.

As shown in Fig. 6f and g, all initial ϕ_{real} values during water flooding are much less than the porosity of the medium (27%), which reconfirms the incomplete sweep of pure solvent flow. Following that, the SAP solution can effectively increase the accessible pore areas piece by piece, as supported by the gradual augment of ϕ_{real} throughout polymer as well as post water injections and a maximum allowable value (~27%) in the end; this behavior parallels our macroscopic core flooding results (Zhang et al., 2019), and give thanks to SAP's adaptive character.

Owing to having close η_{eff} value, a similar profile is observed for HPAM-2 of 750 mg•L^{-1} only after the polymer is injected for 2 pore volume (PV) (Fig. 6g); the ϕ_{real} reduction during the earliest polymer injection may be the result of mild blockage, because the deformation of polymer molecules at this flow rate is already at the beginning of mechanical degradation as shown in Fig. 5a. For high-concentration HPAM-2 solution displacement group (Fig. 6f), the ϕ_{real} value displays a decrease−increase−decrease trend in the course of polymer and post water injection, indicating the processes of plugging, degradation-induced breakthrough, and retention-induced flow direction alteration, because the flow resistance curve manifests this polymer being in the position of stable chain degradation at 10 s^{-1}.

The relatively low-viscosity HPAM-1 solutions, particularly at 1000 mg•L^{-1} (Fig. 6f), show small ϕ_{real} fluctuation, with the value during post water flushing being slightly less than that during initial water flooding, disclosing its poor mobility control ability. This can be attributed to the weak elastic of this kind of polymer, which renders the solution difficult to penetrate into deep and wide zones and mainly rely on absorption on medium surface to lessen pore size. Since increasing the working concentration can boost the amount of absorption and retention to some extent (Sorbie, 1991), the flow of 1250 mg•L^{-1} HPAM-1 solution leads to a detectable decrease in ϕ_{real} value during post water flooding (Fig. 6g).

3.4. Oil displacement by polymer solutions in 3D porous media

The above two-phase flow experiments proved that adaptive polymer has better mobility control ability than M_w-analogous HPAM-1, even at higher concentrations for the latter. While having comparable mobility control power to SAP, plugging and chain degradation are inevitable in HPAM-2 of high weight-average molecular weight. Here, multiple-phase displacement experiments were conducted to intuitively unveil the capacity of these polymer solutions for EOR.

First, paraffin oil having close viscosity to crude oil (Fig. S7 in Electronic Supplementary Material) was used and dyed a different color from water (Fig. S8 in Electronic Supplementary Material), in order to visualizing the dynamic displacement processes. We observe that low-viscosity water soon finds an advantageous flow channel in the oil-saturated medium (Movie S3.mp4 in Electronic Supplementary Material), then the subsequent polymer solution gradually extends the channel to more places, playing a role of mobility control (Movie S4.mp4 in Electronic Supplementary Material).

Supplementary data related to this article can be found at https://doi.org/10.1016/j.petsci.2022.10.013.

Afterwards, crude oil was utilized to implement flooding tests for all polymer solutions. Because crude oil fluoresces at a wide

range of excitation wavelengths (λ_{ex}), it could be distinguished from the medium matrix, the unsaturated pore space, and even the following displacing phase. At $\lambda_{ex} = 488$ nm, as seen in the 3D representation of the oil saturated porous media in Fig. S9a in Electronic Supplementary Material, fluorescent areas in yellow represent oil phase, while black zones relate to the glass beads and the unfilled pore body. Because of the incomplete oil saturation ($S_{oil} \approx 75\%$ see in Table 2), the oil has heterogeneous brightness at different positions and planes, resulting in a wide fluorescence intensity distribution (Fig. S9b in Electronic Supplementary Material).

After oil saturating, the medium was displaced using saline water and polymer solution at a same flow rate as in Section 3.3. Fig. 7 builds the 3D structures of the residual oil after water flooding and post water flushing and coverts them to the fluorescence intensity distribution. From Fig. 7a, one can find that much remaining oil after water flooding keeps the forms of connected ganglia; this is due to the mismatch of viscosity between the displaced phase (11 mPa•s) and the displacing phase (0.6 mPa•s) that generates limited flow pathway. The subsequent polymer and post water sweeping alleviates this trouble to some extent and additional oil is removed (Fig. 7b). The trapped residual oil for SAP displacement group sporadically distributes with less lumped ganglia, revealing a deep intrusion of this adaptive polymer; this is the result of its step-by-step mode of migration as demonstrated in the last section, and also conforms to the apparent blue shift of fluorescence intensity distribution (Fig. 7c). By contrast, the clean of residual oil in other groups seems to do only around the positions that have been created by initial water flooding (labels (2−5) in Fig. 7b), which is highly coincident with the variation in their fluorescence intensity distribution that the location of maximum fluorescence intensity does not shift, with only frequency decrease (labels (2−5) in Fig. 7c).

By comparing the fluorescence intensity distribution of residual oil to that of initial saturated one, we obtain the incremental oil recovery by polymer injection ($E_{p,fluo}$) for the local $640 \times 640 \times 200$ μm^3 volume areas, which is highly consistent with that received from the conventional method of measuring effluent volume (E_p), as tabulated in Table 2. As expected, SAP solution has the higher oil recovery factor (17.8%) than M_w-equivalent HPAM-1 (6.0% and 13.4%), which is attributed to the adaptive feature that gives its deeper access as well as greater elasticity. This difference is also reflected in the pressure drop curves (Fig. S10 in Electronic Supplementary Material); a higher peak pressure during polymer and post water flooding is assigned for SAP than both HPAM-1 solutions. Regarding high-M_w HPAM-2, the moderate clogging and chain degradation as stated before are confirmed again by the excess pressure during polymer injection, as a result, it is difficult to propagate and thus obtain only 10.4% and 8.8% oil recovery.

4. Conclusions

In this work, we fabricated for the first time a medium-

Table 2
Results of oil displacement experiments at 45 °C show concordant polymer enhanced oil recovery obtained from effluent volume calculation (E_p) and fluorescence intensity distribution ($E_{p,fluo}$).

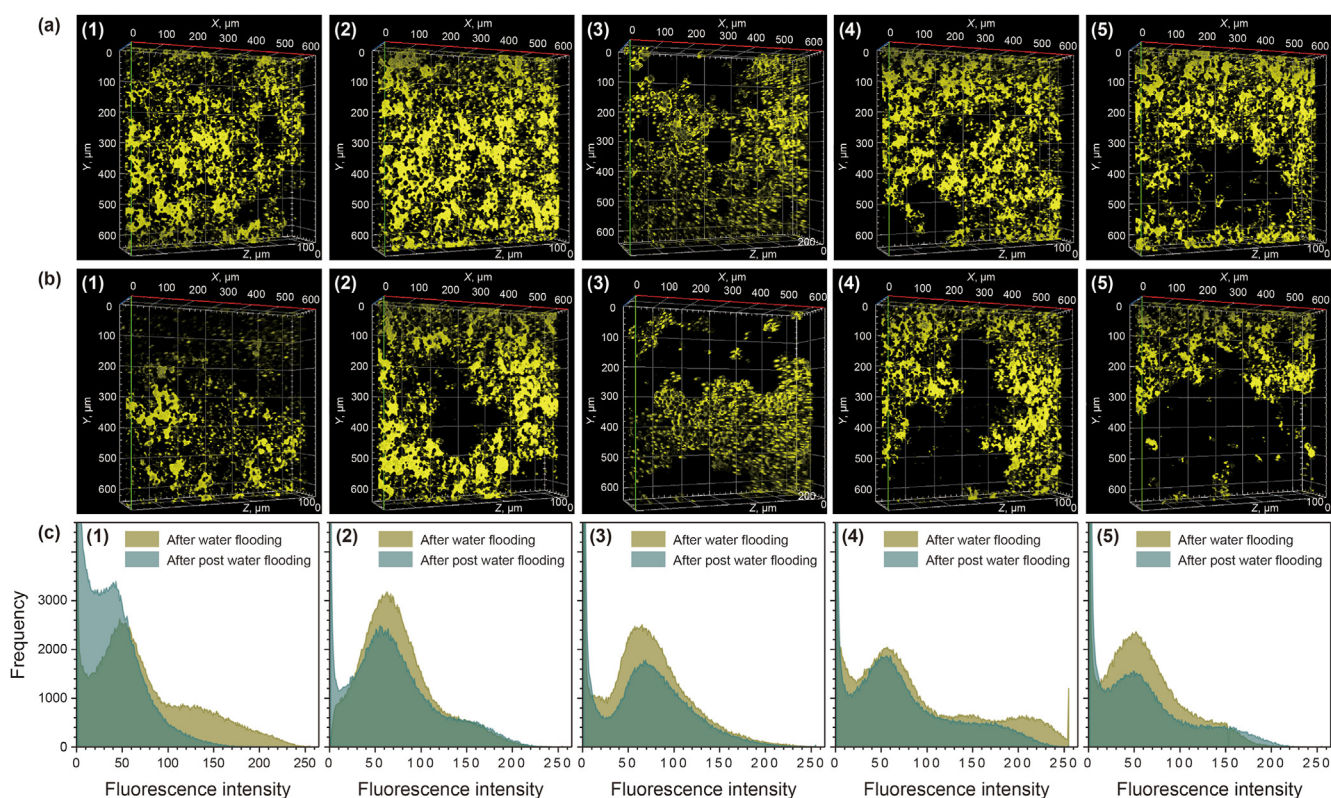| Sample	C_p, mg•L^{-1}	S_{oil}, %	E_w, %	E_p, %	$E_{p,fluo}$, %
SAP	1000	78.5	59.4	15.9	17.8
HPAM-1	1000	73.3	56.5	5.8	6.0
HPAM-2	1000	75.1	59.2	10.2	10.4
HPAM-1	1250	73.3	60.9	11.6	13.4
HPAM-2	750	72.3	57.2	8.5	8.8

Fig. 7. 3D rendering of the residual crude oil (**a**) after water flooding and (**b**) after polymer and post water flooding, which are quantified by (**c**) fluorescence intensity distributions. (1–5) are consecutively for SAP (C_P = 1000 mg•L^{-1}), HPAM-1 (C_P = 1000 mg•L^{-1}), HPAM-2 (C_P = 1000 mg•L^{-1}), HPAM-1 (C_P = 1250 mg•L^{-1}), and HPAM-2 (C_P = 750 mg•L^{-1}) flooding groups. λ_{ex} = 488 nm. Water here is 4500 mg•L^{-1} aqueous solution, which is also the solvent of polymer solution. Displacing fluid was injected continuously along the *X* axis at 45 °C.

permeable core-on-a-chip micromodel towards a more authentic imitation of the realistic reservoir. A comparative study of an adaptive polymer (SAP) and its weight-average molecular weight (M_w)-analogue reference, HPAM-1, as well as an ultra-high-M_w counterpart, HPAM-2, was executed in the semi-dilute regime, with regard to their *in-situ* rheological properties, propagation patterns, and enhanced oil recovery capability. In single-phase flow, increasing the flow rate causes the flow resistance of all polymer solutions to fall first and subsequently increase, with the transition specified by a critical Weissenberg number (Wi_c). SAP has a higher Wi_c than HPAM-1, revealing its extensive shear-governed flow zone. Beyond Wi_c, while HPAM-2 possesses the largest flow resistance, followed by SAP and then HPAM-1, an interval of resistance decrease happens, especially at a higher concentration.

In multiphase displacement, the velocity distribution from PIV measurements was converted to the real-time porosity (ϕ_{real}) which reveals the accessible pore volume of polymer solution. The ϕ_{real} for SAP gradually magnifies in the whole process of displacement, suggesting a piece-by-piece propagation pattern; nevertheless, ϕ_{real} with small fluctuation is observed for HPAM-1, disclosing its poorer mobility control ability than SAP. HPAM-2 of 1000 mg•L^{-1} shows a prominent decline in ϕ_{real} during post water flooding without oil and an excessive pressure during polymer flooding with oil, confirming the occurrence of clogging. Consequently, the maximum recovery factor of 17.8% could be obtained for SAP compared to HPAM-1 (6.0% and 13.4%) and HPAM-2 (10.4% and 8.8%).

These findings uncover the discrepancies of flow dynamics and transportation patterns between adaptive and non-adaptive polymers, which explains the higher oil recovery for SAP in medium-to low-permeability oil reservoirs, and will aid in the design and selection of operating conditions for a target reservoir.

Electronic supplementary material

Descriptions of supplementary Movies. Porosity measurement of the 3D micromodel. Experimental parameters for flow in 3D micromodel. Raw data of bulk shear rheology. Comparison of bulk shear and extensional rheology for polymer solutions in aqueous solution and in index-matching solvent. Velocity distributions for different polymer injection amounts. Choose of fluorescent markers and snapshotting mode for paraffin oil displacement. 3D images and fluorescence intensity distribution of crude oil saturated porous media. Flooding pressure drop in micromodel.

Acknowledgment

Appendix A. Supplementary data

Supplementary data to this article can be found online at https://doi.org/10.1016/j.petsci.2022.10.013.

References

Anbari, A., Chien, H.T., Datta, S.S., Deng, W., Weitz, D.A., Fan, J., 2018. Microfluidic model porous media: fabrication and applications. Small 14, 1703575. https://doi.org/10.1002/smll.201703575.

Azad, M.S., Dalsania, Y.K., Trivedi, J.J., 2018. Capillary breakup extensional rheometry

of associative and hydrolyzed polyacrylamide polymers for oil recovery applications. J. Appl. Polym. Sci. 135, 46253. https://doi.org/10.1002/app.46253.

Azad, M.S., Trivedi, J.J., 2019. Novel viscoelastic model for predicting the synthetic polymer's viscoelastic behavior in porous media using direct extensional rheological measurements. Fuel 235, 218–226. https://doi.org/10.1016/j.fuel.2018.06.030.

Bennetzen, M.V., Gilani, S.F., Mogensen, K., Ghozali, M., Bounoua, N., 2014. Successful polymer flooding of low-permeability, oil-wet, carbonate reservoir cores. In: Abu Dhabi International Petroleum Exhibition and Conference. https://doi.org/10.2118/171849-MS.

BP p.l.c., 2022. Statistical Review of World Energy. https://www.bp.com/content/dam/bp/business-sites/en/global/corporate/pdfs/energy-economics/statistical-review/bp-stats-review-2022-full-report.pdf. (Accessed 11 July 2022).

Browne, C.A., Datta, A.A., 2021. Elastic turbulence generates anomalous flow resistance in porous media. Sci. Adv. 7, eabj2619. https://doi.org/10.1126/sciadv.abj2619.

Browne, C.A., Shih, A., Datta, A.A., 2020. Pore-scale flow characterization of polymer solutions in microfluidic porous media. Small 16, 1903944. https://doi.org/10.1002/smll.201903944.

Carreau, P.J., 1972. Rheological equations from molecular network theories. Trans. Soc. Rhea. 16, 99–127. https://doi.org/10.1122/1.549276.

Chauveteau, G., 1982. Rodlike polymer solution flow through fine pores: influence of pore size on rheological behaviors. J. Rheol. 26, 111–142. https://doi.org/10.1122/1.549660.

Chissonde, S., Azad, M.S., Trivedi, J., 2021. Flow of hydrophobically associating polymers through unconsolidated sand pack: role of extensional rheology and degree of association. J. Mol. Liq. 344, 117643. https://doi.org/10.1016/j.molliq.2021.117643.

China National Energy Administration, 2021. Classification for Oil Reservoir. Chinese Standard SY/T 6169–1995 (in Chinese).

Datta, S.S., Chiang, H., Ramakrishnan, T.S., Weitz, D.A., 2013. Spatial fluctuations of fluid velocities in flow through a three-dimensional porous medium. Phys. Rev. Lett. 111, 064501. https://doi.org/10.1103/PhysRevLett.111.064501.

Datta, S.S., Dupin, J.P., Weitz, D.A., 2014a. Fluid breakup during simultaneous two-phase flow through a three-dimensional porous medium. Phys. Fluids 26, 062004. https://doi.org/10.1063/1.4884955.

Datta, S.S., Ramakrishnan, T.S., Weitz, D.A., 2014b. Mobilization of a trapped non-wetting fluid from a three-dimensional porous medium. Phys. Fluids 26, 022002. https://doi.org/10.1063/1.4866641.

Dinic, J., Zhang, Y., Jimenez, L.N., Sharma, V., 2015. Extensional relaxation times of dilute, aqueous polymer solutions. ACS Macro Lett. 4, 804–808. https://doi.org/10.1021/acsmacrolett.5b00393.

Dinic, J., Jimenez, L.N., Sharma, V., 2017. Pinch-off dynamics and dripping-onto-substrate (DoS) rheometry of complex fluids. Lab Chip 17, 460–473. https://doi.org/10.1039/C6LC01155A.

Dupuis, G., Rousseau, D., Tabary, R., Grassl, B., 2011. Flow of hydrophobically modified water-soluble-polymer solutions in porous media: new experimental insights in the diluted regime. SPE J. 16, 43–54. https://doi.org/10.2118/129884-PA.

Entov, V.M., Hinch, E.J., 1997. Effect of a spectrum of relaxation times on the capillary thinning of a filament of elastic liquid. J. Non-Newtonian Fluid Mech. 72, 31–54. https://doi.org/10.1016/S0377-0257(97)00022-0.

Galindo-Rosales, F.J., Campo-Deaño, L., Pinho, F.T., Bokhorst, E.V., Hamersma, P.J., Oliveira, M.S.N., Alves, M.A., 2012. Microfluidic systems for the analysis of viscoelastic fluid flow phenomena in porous media. Microfluid. Nanofluidics 12, 485–498. https://doi.org/10.1007/s10404-011-0890-6.

González, J.M., Müller, A.J., Torres, M.F., Sáez, A.E., 2005. The role of shear and elongation in the flow of solutions of semi-flexible polymers through porous media. Rheol. Acta 44, 396–405. https://doi.org/10.1007/s00397-004-0421-4.

Guo, Y., Hu, J., Zhang, X., Feng, R., Li, H., 2016. Flow behavior through porous media and microdisplacement performances of hydrophobically modified partially hydrolyzed polyacrylamide. SPE J. 21, 688–705. https://doi.org/10.2118/178921-PA.

Guo, Y., Liang, Y., Cao, M., Feng, R., Zhang, X., Li, H., Hu, J., 2017. Flow behavior and viscous-oil- microdisplacement characteristics of hydrophobically modified partially hydrolyzed polyacrylamide in a repeatable quantitative visualization micromodel. SPE J. 22, 1448–1466. https://doi.org/10.2118/185185-PA.

Hatzignatiou, D.G., Moradi, H., Stavland, A., 2013. Experimental investigation of polymer flow through water and oil-wet Berea sandstone core samples. In: EAGE Annual Conference & Exhibition Incorporating SPE Europec. https://doi.org/10.2118/164844-MS.

Haynes, A.K., Clough, M.D., Fletcher, A.J., Weston, S., 2013. The successful implementation of a novel polymer EOR pilot in the low permeability Windalia field. In: SPE Enhanced Oil Recovery Conference. https://doi.org/10.2118/165253-MS.

Ibezim, V.C., Poole, R.J., Dennis, D.J.C., 2021. Viscoelastic fluid flow in microporous media. J. Non-Newtonian Fluid Mech. 296, 104638. https://doi.org/10.1016/j.jnnfm.2021.104638.

Jones, M., 1963. Water-flooded mobility control: a case history. J. Petrol. Technol. 18, 1151–1156. https://doi.org/10.2118/1427-PA.

Karadimitriou, N.K., Hassanizadeh, S.M., 2012. A review of micromodels and their use in two-phase flow studies. Vadose Zone J. 11. https://doi.org/10.2136/vzj2011.0072 vzj2011.0072.

Krummel, A.T., Datta, S.S., Münster, S., Weitz, D.A., 2013. Visualizing multiphase flow and trapped fluid configurations in a model three-dimensional porous medium. AIChE J. 59, 1022–1029. https://doi.org/10.1002/aic.14005.

Leon, J.M., Castillo, A.F., Perez, R., Jimenez, J.A., Izadi, M., Mendez, A., Castillo, O.P., Londoño, F.W., Zapata, J.F., Chaparro, C.H., 2018. A successful polymer flood pilot at Palogrande-Cebu, a low permeability reservoir in the upper Magdalena valley, Colombia. In: SPE Improved Oil Recovery Conference. https://doi.org/10.2118/190165-MS.

Lewandowska, K., 2007. Comparative studies of rheological properties of polyacrylamide and partially hydrolyzed polyacrylamide solutions. J. Appl. Polym. Sci. 103, 2235–2241. https://doi.org/10.1002/app.25247.

Li, X., Xu, Z., Yin, H.Y., Feng, Y.J., Quan, H.P., 2017. Comparative studies on enhanced oil recovery: thermoviscosifying polymer versus polyacrylamide. Energy Fuel. 31, 2479–2487. https://doi.org/10.1021/acs.energyfuels.6b02653.

Martínez Narváez, C.D.V., Dinic, J., Lu, X., Wang, C., Rock, R., Sun, H., Sharma, V., 2021. Rheology and pinching dynamics of associative polysaccharide solutions. Macromolecules 54, 6372–6388. https://doi.org/10.1021/acs.macromol.0c02751.

McKinley, G.H., 2005. Visco-elasto-capillary thinning and break-up of complex fluids. Rheol. Rev. 1–48. 05-P-04. http://hdl.handle.net/1721.1/18085.

Mezger, T., 2020. The Rheological Handbook. Vincentz Network, Hannover. https://doi.org/10.1515/9783748603702.

Nilsson, M.A., Kulkarni, R., Gerberich, L., Hammond, R., Singh, R., Baumhoff, E., Rothstein, J.P., 2013. Effect of fluid rheology on enhanced oil recovery in a microfluidic sandstone device. J. Non-Newtonian Fluid Mech. 202, 112–119. https://doi.org/10.1016/j.jnnfm.2013.09.011.

Ober, T.J., Haward, S.J., Pipe, C.J., Soulages, J., McKinley, G.H., 2013. Microfluidic extensional rheometry using a hyperbolic contraction geometry. Rheol. Acta 52, 529–549. https://doi.org/10.1007/s00397-013-0701-y.

Oliveira, M.S.N., Yeh, R., McKinley, G.H., 2006. Iterated stretching, extensional rheology and formation of beads-on-a-string structures in polymer solutions. J. Non-Newton Fluid 137, 137–148. https://doi.org/10.1016/j.jnnfm.2006.01.014.

Parsa, S., Santanach-Carreras, E., Xiao, L., Weitz, D.A., 2020. Origin of anomalous polymer-induced fluid displacement in porous media. Phys. Rev. Fluids 5, 022001. https://doi.org/10.1103/PhysRevFluids.5.022001.

Parsa, S., Zareei, A., Santanach-Carreras, E., Morris, E.J., Amir, A., Xiao, L., Weitz, D.A., 2021. Unexpected scaling of interstitial velocities with permeability due to polymer retention in porous media. Phys. Rev. Fluids 6, L082302. https://doi.org/10.1103/PhysRevFluids.6.L082302.

Pipe, C.J., Majmudar, T.S., McKinley, G.H., 2008. High shear rate viscometry. Rheol. Acta 47, 621–642. https://doi.org/10.1007/s00397-008-0268-1.

Pu, H., Yin, D., Chen, Y., Yang, F., 2008. Feasibility study and pilot test of polymer flooding in third class Reservoir of Daqing oilfield. In: SPE North Africa Technical Conference & Exhibition. https://doi.org/10.2118/111720-MS.

Ranjbar, M., Rupp, J., Pusch, G., Meyn, R., 1992. Quantification and optimization of viscoelastic effects of polymer solutions for enhanced oil recovery. In: SPE/DOE Enhanced Oil Recovery Symposium. https://doi.org/10.2118/24154-MS.

Rodd, L.E., Cooper-White, J.J., Boger, D.V., McKinley, G.H., 2007. Role of the elasticity number in the entry flow of dilute polymer solutions in micro-fabricated contraction geometries. J. Non-Newtonian Fluid Mech. 143, 170–191. https://doi.org/10.1016/j.jnnfm.2007.02.006.

Rodd, L.E., Scott, T.P., Cooper-White, J.J., McKinley, G.H., 2005. Capillary break-up rheometry of low-viscosity elastic fluids. Appl. Rheol. 15, 12–27. https://doi.org/10.1515/arh-2005-0001.

Seright, R.S., 1983. The effects of mechanical degradation and viscoelastic behavior on injectivity of polyacrylamide solutions. SPE J. 23, 475–485. https://doi.org/10.2118/9297-PA.

Seright, R.S., Fan, T., Wavrik, K., de Carvalho Balaban, R., 2011. New insights into polymer rheology in porous media. SPE J. 16, 35–42. https://doi.org/10.2118/129200-PA.

Skauge, A., Zamani, N., Jacobsen, J.G., Shiran, B.S., Al-Shakry, B., Skauge, T., 2018. Polymer flow in porous media: relevance to enhanced oil recovery. Colloids Interfaces 2, 1–27. https://doi.org/10.3390/colloids2030027.

Smith, F.W., 1970. The behavior of partially hydrolyzed polyacrylamide solutions in porous media. J. Petrol. Technol. 22, 148–156. https://doi.org/10.2118/2422-PA.

Sochi, T., 2010. Non-Newtonian flow in porous media. Polymer 51, 5007–5023. https://doi.org/10.1016/j.polymer.2010.07.047.

Sorbie, K.S., 1991. Polymer-improved Oil Recovery. CRC Press, Boca Raton. https://doi.org/10.1007/978-94-011-3044-8_1.

Sousa, P.C., Pinho, F.T., Alves, M.A., 2018. Purely-elastic flow instabilities and elastic turbulence in microfluidic cross-slot devices. Soft Matter 14, 1344–1354. https://doi.org/10.1039/C7SM01106G.

Stavland, A., Jonsbråten, H.C., Lohne, A., Moen, A., Giske, N.H., 2010. Polymer flooding: flow properties in porous media versus rheological parameters. In: SPE EUROPEC/EAGE Annual Conference and Exhibition, 14–17 June, Barcelona. https://doi.org/10.2118/131103-MS.

Thomas, A., 2016. Polymer flooding. In: Romero-Zerón, L. (Ed.), Chemical Enhanced Oil Recovery (cEOR)-A Practical Overview. Intech, Rijeka, pp. 55–99. https://doi.org/10.5772/64623.

Wang, J., Shi, L., Zhu, S., Xiong, Y., Liu, Q.Y., 2021. Effect of hydrophobic association on the flow resistance of polymer solutions. AIP Adv. 11, 065324. https://doi.org/10.1063/5.0050321.

Wever, D.A.Z., Picchioni, F., Broekhuis, A.A., 2011. Polymers for enhanced oil recovery: a paradigm for structure-property relationship in aqueous solution. Prog. Polym. Sci. 36, 1558–1628. https://doi.org/10.1016/j.progpolymsci.2011.05.006.

Willhite, G.P., 1986. Waterflooding, third ed. Society of Petroleum Engineers, Richardson. https://doi.org/10.2118/9781555630058.

Wu, S., 2013. Shear and elongational rheology of partially hydrolyzed poly-acrylamide used for enhanced oil recovery. Appl. Rheol. 23, 53800. https://doi.org/10.3933/applrheol-23-53800.

Zamani, N., Bondino, I., Kaufmann, R., Skauge, A., 2015. Effect of porous media properties on the onset of polymer extensional viscosity. J. Pet. Sci. Eng. 133, 483−495. https://doi.org/10.1016/j.petrol.2015.06.025.

Zhang, X., Li, B., Pan, F., Su, X., Feng, Y., 2021. Enhancing oil recovery from low-permeability reservoirs with a thermoviscosifying water-soluble polymer. Molecules 26, 7468. https://doi.org/10.3390/molecules26247468.

Zhang, Y., Feng, Y., Li, B., Han, P., 2019. Enhancing oil recovery from low-permeability reservoirs with a self-adaptive polymer: a proof-of-concept study. Fuel 251, 146−156. https://doi.org/10.1016/j.fuel.2019.04.034.

Zhao, X.D., Dong, M.Z., Maini, B., 2013. The dominant mechanism of enhanced heavy oil recovery by chemical flooding in a two-dimensional physical model. Fuel 108, 261−268. https://doi.org/10.1016/j.fuel.2013.02.012.

Zhao, X.Z., Liao, G.Z., Gong, L.Y., Luan, H.X., Chen, Q.S., Liu, W.D., Liu, D., Feng, Y.J., 2022. New insights into the mechanism of surfactant enhanced oil recovery: micellar solubilization and in-situ emulsification. Petrol. Sci. 19, 870−881. https://doi.org/10.1016/j.petsci.2021.11.014.